Experiments in Fluids 31 (2001) 140–152 © Springer-Verlag 2001

Simultaneous velocity and concentration measurements in the near field of a turbulent low-pressure jet by digital particle image velocimetry–planar laser-induced fluorescence

A. Borg, J. Bolinder, L. Fuchs

Abstract The main purpose of this work is to develop a method for simultaneous measurement of velocity and passive scalar concentration by means of digital particle image velocimetry and planar laser-induced fluorescence. Details of the implementation of the method are given, and the technique is applied to measurements of concentration and velocity in the centre-plane of a liquid jet with a Reynolds number of 6,000. The measurements are compared with large eddy simulations. Mean velocities and concentrations, fluctuating velocities and concentrations, and correlation between fluctuating velocities and concentrations are analysed for the first six diameters downstream of the jet exit. The general agreement between measured and simulated results was found to be good, in particular for mean quantities. Mean profiles are also found to be in good agreement with other experimental work on jets reported in the literature. The "whole-plane" measurement method was found to be very useful for detailed comparisons of turbulent statistics with simulated data. The inadequacy of models for turbulent mass transport based on the standard gradient diffusion concept is demonstrated through the experimental data.

1 Introduction

Coupled diffusion–convection of a scalar quantity, such as temperature or concentration is relevant for many processes, such as mixing in combustion chambers or distribution of drugs in biomedical applications. The possibility of measuring velocity and a scalar simultaneously with a high spatial and/or temporal resolution is of fundamental importance for the validation and development of numerical models of turbulence and turbulent mixing. Simultaneous measurements of velocity and concentration allow the determination of the correlation of fluctuating velocity and fluctuating concentration, which offers the possibility of determining the validity of different models for turbulent mass transport. The experimental method employed here provides velocity and concentration in a plane at the same time instant. This has several advantages over single point measurements: Two-dimensional data allow the identification of coherent structures present in the flow, and turbulent statistics which are calculated by ensemble averaging over a set of flow field images are available in the full plane. Simultaneous instantaneous velocity and concentration data in a plane allow the validation of turbulence models based on spatial filtering [sub-grid scale (SGS), terms in large eddy simulations (LES)] as well as providing experimental data for the turbulent concentration fluxes. A good example of utilising PIV data for this kind of analysis is the paper by Liu et al. (1994), in which it is shown that eddy-viscosity closures of the Smagorinsky type show very low correlation with the real sub-grid scale stress. For highly resolved simultaneous velocity and concentration measurements (beyond the Taylor micro-scale), the same type of testing can be done for models of SGS mixing. This work utilises particle image velocimetry (PIV) for velocity measurements and laser-induced fluorescence (LIF) for concentration measurements. Examples of earlier work on measurements of concentration and velocity in a turbulent jet include the measurements by Lemoine et al. (1996). They performed simultaneous one-point measurements by LIF and laser Doppler velocimetry (LDV), for a submerged turbulent water jet at $Re = 5{,}500$. A technique close to the one adopted in this paper was used by Sakakibara et al. (1997) to measure the velocity and temperature of an impinging plane jet. They used a fluorescing dye with strong temperature dependence (Rhodamine B) to measure temperature. Their technique differs from ours in the implementation and in details of the post-processing as will be discussed below.

The success of the combination of PIV and PLIF is to a large extent determined by the proper implementation of the two techniques separately. An additional difficulty when doing the combined measurement is the alignment of the cameras so that they view the same region in space. Some interpolation scheme is required to match the position of the velocity and concentration data. Techniques to handle this are presented in the paper. The measurement method and the numerical simulation procedure presented in this paper are applied to study the near field of a circular turbulent jet. A short description of the physical properties of this particular flow is as follows.

The circular jet is a model problem for axisymmetric turbulent shear flow. The circular jet was studied for decades

Received: 4 October 2000/Accepted: 27 November 2000

A. Borg, J. Bolinder, L. Fuchs (✉)
Department of Heat and Power Engineering
Division of Fluid Mechanics, Lund Institute of Technology
Box 118, 22100 Lund, Sweden
e-mail: Laszlo.Fuchs@vok.Lth.se

Financial support by TFR, the Swedish Research Council for Engineering Sciences, is very gratefully acknowledged.

and its properties are rather well known. The following description of the near-field dynamics of the turbulent jet is given by Danaila et al. (1997): "For a large range of Reynolds numbers ($5{,}500 < Re < 10^6$) the scenario of the early stages of evolution of the round jet seems to be universal (independent of the Reynolds number): the shear layer origin from the inlet (nozzle or pipe exit) is inviscidly unstable via a Kelvin–Helmolz primary instability; the instability grows downstream and rolls up into coherent vortex rings; the structures merge as they are convected downstream. Streamwise vortex structures develop through a secondary three-dimensional instability of the thin vorticity layer between two neighbouring vortex rings."

The primary aim of this study is to present a method of simultaneously measuring velocity and concentration in a plane, and the current measurements are used to assess turbulent statistics in the near inlet region of a turbulent jet (0–6 D). The results are compared with simulated results of the same flow with large eddy simulations. Comparison with some earlier experimental data is also made. The experimental data are used to point out conceptual weaknesses in a commonly used gradient diffusion model for turbulent mass transport.

2 Methods

2.1 Concentration measurements by PLIF

The principle of planar laser-induced fluorescence (PLIF) is to excite a particular electronic transition of a molecular tracer with a laser sheet whose frequency is tuned to cause excitation. In the present investigation, we use Rhodamine B as a tracer, which is excited by the second harmonic (532 nm) from a pulsed Nd:YAG laser. The dye then emits broadband fluorescence with a peak around 590 nm, and the fluorescence is captured by a CCD camera with a high-pass filter (>550 nm) to remove scattered light. To describe the process of how the detected emission at each pixel in the digital camera array depends on local concentration for each laser pulse, we follow van Cruyningen et al. (1990). The process can be divided into three steps: a number of photons are emitted; of these a number of photons reach the collecting optics; and finally conversion into a digital signal. For unsaturated excitation and constant properties of the carrier fluid (temperature, oxygen content, pH value) the total light emission per unit sheet area is given by:

$$\begin{aligned} N''_{\mathrm{e}}(x,y,v,t) &= \{\text{photons incident per unit height}\} \\ &\quad \{\text{photons absorbed per unit length}\} \\ &\quad \{\text{photons emitted per photons absorbed}\} \\ &= \left\{N'_i(y)\mathrm{e}^{-(\alpha(v)+\sigma)\int c(x,y)\mathrm{d}x}\right\}\{\alpha(v)c(x,y)\} \\ &\quad \{\eta(v,t)\} \end{aligned} \tag{1}$$

where $N''_{\mathrm{e}}(x,y,v,t)$ denotes photons per unit area at a position in space as a function of time t and frequency v, $N'_i(y)$ is the number of photons per unit height in cm^{-1} from the laser, $\alpha(v)$ is the absorbing cross-section of the tracer in cm^2, σ is the Rayleigh scattering section of the tracer in cm^2, $c(x, y)$ is the concentration of the absorbing species in the lower energy level in cm^{-3}, $\eta(v, t)$ is the species quantum efficiency for the transition (see van Cruyningen et al. 1990). For a pulsed laser, the energy will vary from pulse to pulse both in an integral sense (total energy variation) and in the distribution over the laser sheet. If the concentration level is low enough, Eq. (1) becomes linear in the species concentration. The collection optics has the purpose of imaging the fluorescence emission on the light-sensitive camera array. The amount of light reaching the camera and its spectral content depend on the camera lenses, the filter to remove scattered laser light, the magnification and the limiting aperture. The number of photons per pixel reaching the camera is given by:

$$\begin{aligned} &N_{\mathrm{pp}}(x,y,v,t) \\ &\quad = \{\text{emission per unit area}\}\{\text{area}\}\left\{\frac{\text{solid angle}}{4\pi}\right\} \\ &\qquad \{\text{gain or loss}\}\{\text{spectral filter}\}\{\text{temporal filter}\} \\ &\qquad \{\text{optical factors}\} \\ &\quad = \left\{N'_{\mathrm{e}}(x,y,v,t) + N''_{\mathrm{b}}(x,y,v,t)\right\}\left\{L_x L_y\right\}\left\{\frac{\pi r_l^2}{4\pi z_l^2}\right\} \\ &\qquad \{GF(v)T(t)\mathrm{H}(x,y,v)\} \end{aligned} \tag{2}$$

where $N''_{\mathrm{b}}(x,y,v,t)$ is the background emission per unit area, L_x and L_y are the dimensions of a pixel in the measuring plane and are related to the pixel size l_{p} by $L_x = l_{\mathrm{p}}/M$, where M is the magnification, r_{l} is the radius of the limiting aperture, z_{l} is the distance from the laser-sheet to the limiting aperture, G accounts for losses from lens and filter surfaces, $F(v)$ takes into account the filtering of the signal, $T(t)$ is the time transfer function of the camera, and $H(x, y, v)$ takes into account additional optical effects (non-ideal optics). The final signal obtained in each pixel for each laser pulse is given by integration over the time the array is exposed to light and by integration over frequency (due to the frequency sensitivity of the CCD-chip). For fixed optical settings in the linear range, the following simplified equation holds for the digital signal level $i_{\mathrm{d}}(x, y, n)$ in each pixel for each laser pulse:

$$i_{\mathrm{d}}(x,y,n) = k(x,y,n)c(x,y,n) + i_{\mathrm{db}}(x,y,n) \tag{3}$$

In this equation $k(x, y, n)$ includes variations in laser energy over the sheet for pulse n and the optical factors discussed above and, as we measure the concentration of Rhodamine B in μg/l, it has the unit of l/μg. $i_{\mathrm{db}}(x, y, n)$ is the background emission and depends on optical factors and variations in the background but not on the laser energy if scattered light is effectively filtered out. The optical factors are constant but, to be able to measure the instantaneous concentration, the laser energy in each pulse must be measured over the sheet height. The rms fluctuation in the total irradiance from pulse to pulse is typically some percentage of the mean. Since we do not measure the

laser energy, an error is introduced in the instantaneous concentration data processing due to the pulse-to-pulse variation. This is discussed further below. For Eq. (3) to be valid, it is important that the intensity is linear in concentration, that absorption effects are negligible and that absorption does not depend on laser intensity. In a recent paper, Karasso and Mungal (1997) ruled out sodium fluorescein as a dye candidate in combination with the pulsed Nd:YAG laser due to violation of Beer's law. We studied our laser and dye combination with respect to this effect. Uniform solutions of Rhodamine B with concentrations of 192, 96 and 48 μg/l, respectively, were investigated in a rectangular box. A light-sheet similar to the one used in the jet experiment was formed (thickness 1.5 mm, height 5 cm, low angle of divergence, 25 mJ per pulse). The intensity along the beam-path was then measured with the CCD camera. To eliminate optical effects, the receiving optics is moved with respect to the laser sheet in steps of 5 mm and the recorded intensity is compared at a fixed position in the CCD-array. Figure 1 (upper frame) shows the logarithm of the intensity (normalised with its value at $x = 0$) along the beam-path for the three different concentrations investigated (background subtracted). According to Beer's law, this variation should be linear and the absorption should increase linearly with concentration, which is clearly seen in the figure. In the jet experiments, the maximum concentration used is 15 μg/l. It is clearly seen in Fig. 1 that the absorption at this concentration level is very low for the beam-paths used in the jet experiment (smaller than 20 cm). The lower frame in Fig. 1 shows the logarithm of the intensity (normalised with its value at $x = 0$) along the beam path for the concentration of 192 μg/l at two different positions in the laser sheet with different intensities. This shows that the absorption is only very weakly dependent on laser energy for the pulse energies used in the experiment.

The following procedure is employed for calibration of the concentration measurements. First, the mean background emission I_{db} in each pixel is determined by acquisition of 20 images of a field with no dye present but with scattering particles and the laser running. Thereafter, the mean corrected intensity I_{dc} (mean background emission subtracted) is used to determine the mean coefficient $K(x, y)$ in each pixel as an average over 20 images of six known concentrations in the linear range (0–15 μg/l). Taking the ensemble average of Eq. (3) for a constant concentration gives the following equation (capitals denote ensemble averaged quantities):

$$I_{dc}(x,y) = I_d(x,y) - I_{db}(x,y) = K(x,y)c \tag{4}$$

The constant $K(x, y)$ is determined by a least square fit to Eq. (4) over the tested concentrations, i.e.

$$K(x,y)\sum_{i=1}^{N} c_i^2 = \sum_{i=1}^{N} c_i (I_{dc}(x,y))_i \tag{5}$$

where N denotes the number of tested concentrations.

Figure 2 shows the detected intensities versus concentration and the corresponding linear fit at a position in the camera array. The mean uncertainty in the parameter $K(x, y)$ is 5% (with 95% confidence). The measured instantaneous concentration $c_m(x, y)$ is given by the following equation:

$$c_m(x,y) = \frac{i_{dc}(x,y)}{K(x,y)} = c(x,y) + \frac{k'(x,y)}{K(x,y)}c(x,y) + \frac{i'_{db}(x,y)}{K(x,y)} \tag{6}$$

The rms values of k' and i'_{db} are determined as an average over the array. The variance of i_{dc}/K versus the square of the concentration shows linear behaviour. Using these data, we found that the laser energy variation is about 2.5% of the mean energy and that the variation in the background corresponds to a concentration of 0.1 μg/l, which is 1% of the inlet concentration used in the jet experiment.

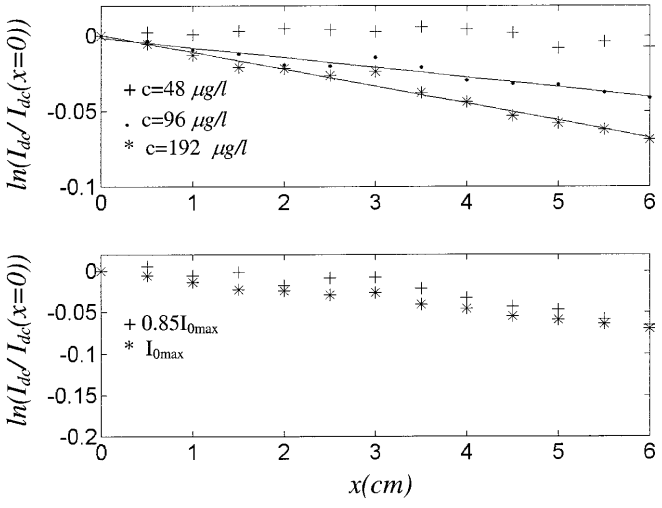

Fig. 1. Validation of Beer's law. Intensity versus beam-path for three different concentrations (*upper chart*) and intensity versus beam-path for two different places in the laser sheet with different entrance intensities (*lower chart*, $I_0 = I_{0max}$ and $I_0 = 0.85I_{0max}$)

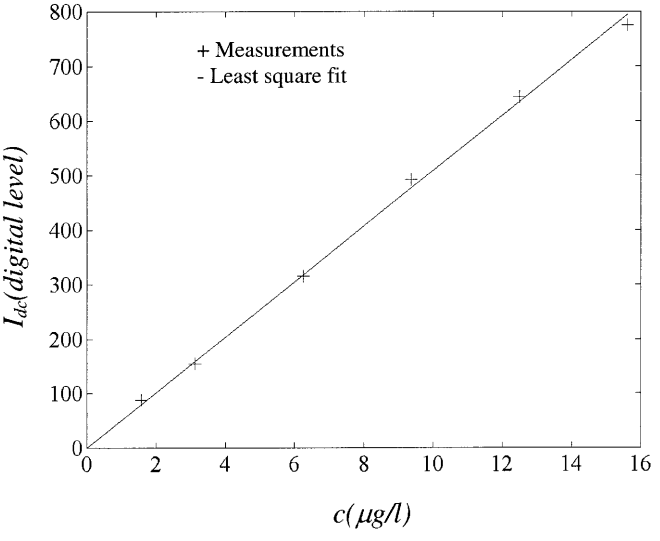

Fig. 2. LIF-pixel intensity versus concentration at an arbitrary position in the camera array together with the linear least square fit

The laser intensity fluctuations and the background fluorescent light fluctuations are independent of each other. This fact can be used to improve the estimation of the turbulent statistics involving concentration. The measured mean value is not affected by the fluctuations as can be seen from:

$$\overline{c_{\mathrm{m}}} = \frac{\overline{(K+k')c + i''_{\mathrm{db}}}}{K} = \overline{c} \tag{7}$$

The measured concentration fluctuations are effected by the laser and background fluctuations and are related to the real concentration fluctuations by the following equation:

$$\begin{aligned}
\overline{c'^2_{\mathrm{m}}} &= \overline{(c_{\mathrm{m}} - \overline{c_{\mathrm{m}}})^2} = \overline{\left(\frac{(K+k')(\overline{c}+c') + i'_{\mathrm{db}}}{K} - \overline{c}\right)^2} \\
&= \overline{\left(c' + \frac{k'(\overline{c}+c') + i'_{\mathrm{db}}}{K}\right)^2} \\
&= \overline{c'^2} + \overline{2c'\left(\frac{k'(\overline{c}+c') + i'_{\mathrm{db}}}{K}\right)} + \overline{\left(\frac{k'}{K}\right)^2(\overline{c}^2 + 2\overline{c}c' + c'^2)} \\
&\quad + \frac{\overline{2i'_{\mathrm{db}}k'(\overline{c}+c')}}{K} + \overline{\left(\frac{i'_{\mathrm{db}}}{K}\right)^2} \\
&= \overline{\left(\frac{k'}{K}\right)^2}\,\overline{c}^2 + \overline{\left(\frac{k'}{K}\right)^2}\,\overline{c'^2} + \overline{\left(\frac{i'_{\mathrm{db}}}{K}\right)^2} + \overline{c'^2}
\end{aligned} \tag{8}$$

This relation is used to improve the estimation of the concentration fluctuations. The velocity–concentration correlation is not affected by fluctuations in laser energy or in the background, if it assumed that these stochastic processes are independent, since:

$$\begin{aligned}
\overline{(u'c')_{\mathrm{m}}} &= \overline{u'\left(\frac{(K+k')(\overline{c}+c') + i'_{\mathrm{db}}}{K} - \overline{c}\right)} \\
&= \overline{u'\left(c' + \frac{k'}{K}(\overline{c}+c') + \frac{i'_{\mathrm{db}}}{K}\right)} = \overline{u'c'}
\end{aligned} \tag{9}$$

We tested the algorithm on a laminar jet for which the core concentration is constant for long distances. It was found that the centreline concentration varied less than 5% in that laminar jet, and that the procedure described above reduced the measured concentration fluctuations in the jet due to laser and background fluctuations below 1%.

2.2 Velocity measurements by DPIV

The general principle of PIV is to illuminate tracer particles in the flow field with a plane sheet of light, and to acquire two images of the scattered light from the particles with a known time separation. In PIV, the displacement field is determined as an average displacement within a so-called interrogation area of the image plane during the known time separation between the acquisition of the two images. An FFT-based cross-correlation is used to determine the average displacement in the interrogation area. Sub-pixel interpolation is done with a Gaussian peak fit, see Raffel et al. (1998). The present algorithm utilises local window shifting and bias correction. Local window shifting was shown to reduce the measurement noise (rms error) and is described by Westerweel et al. (1997). An initial pass with a larger interrogation cell size is used, which gives more reliable displacements due to the higher particle image density. For the present measurement an initial cell size of 32 pixels and a final cell size of 16 pixels with a 50% overlap was used. For the post-processing of the vector fields, a local median test was used to remove stray vectors. In the local median test, the median velocity in a 3×3 region around the vector to be tested was first computed. This was done individually for each component. The allowed deviation from the median was fixed for the whole vector field to 2 pixels for both components. If the highest correlation peak did not pass the median test, the next highest peak was tested and so forth down to the fourth highest peak. Places where no acceptable vector could be found were filled up with the average of the neighbouring eight vectors. The median test was repeated once with a filling-up pass in between. No smoothing of the vector fields was done. The uncertainty in the displacement calculation is estimated to 0.1–0.5 pixels, which for a maximum displacement of around 6 pixels gives an accuracy (in uniform flow regions) of at best 1.5% for the velocity estimate.

2.3 Flow system and instrumentation

The geometry of the experimental set-up is shown in Fig. 3, with the employed coordinate axes indicated. The jet box and the jet pipe are made by Plexi-glass. An elevated tank supplies the necessary head to drive the system, and the pipe has an inner diameter of 10 mm, the wall is 0.5 mm thick and 1 m long. This length is sufficient to make the outlet profile fully developed turbulent. The box has the dimensions of $H = 1.2$ m and $B = 0.28$ m. During the experiment the water surface is located 10 cm above the pipe exit. Water at a temperature of 12 °C is used and

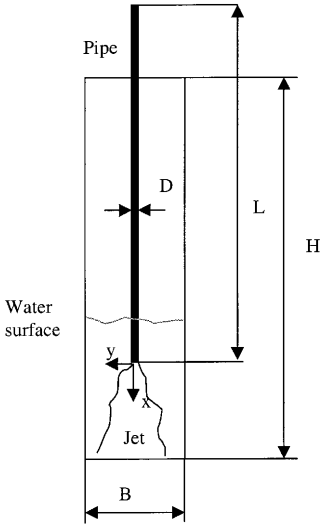

Fig. 3. Sketch of the experimental set-up

the mean cross-sectional velocity in the pipe is 0.75 m/s. In terms of non-dimensional parameters, the flow can be described by the Reynolds number $Re = 6{,}000$ and the Schmidt number $Sc = O(1{,}000)$. The concentration of Rhodamine B was close to 10 μg/l in all runs.

A modified commercial system (LaVision) is used for DPIV and PLIF measurements. It consists of two high-resolution (1,280 × 1,024), 12-bit, cross-correlation CCD cameras mounted on a plate, with a beam splitter and a mirror to split the incoming light between the cameras. The light source is a double-cavity 25 mJ Nd:YAG laser with a maximum repetition rate of 15 Hz. Optical high- and low-pass filters are placed in front of the cameras so that one camera detects the fluorescence of Rhodamine B, and the other detects scattered light from the particles. The principal set-up is shown in Fig. 4.

For the PIV camera, the following parameters hold: 1 pixel corresponds to 37 μm in the measurement plane, which means that a measurement covers about three and a half pipe diameters. An interrogation cell size of 16 pixels is used with an overlap of 50%. This means that we get 34 vectors across the span of the pipe (though not representing fully independent measurements). The light-sheet thickness is about 1 mm, and the measurement volume has dimensions of 0.6 × 0.6 × 1 mm. This volume is adequate, since we expect that the out-of-plane motion is of the same order of magnitude as the in-plane motion. With an image magnification $M = 0.18$ and a numerical aperture $f^{\#} = 8$, the depth of field is about 7 mm, which is wider than the light-sheet thickness. The flow is seeded with hollow glass particles around 10 μm in size. The particle image density is about eight per interrogation area, computed with a threshold set to three times the background noise level, and the particle image diameter is about 3.5 pixels. For the camera that detects the LIF signal, binning of 4 pixels to one is done, resulting in an effective pixel dimension of 74 μm. The numerical aperture for this camera is 2.8, giving an estimated depth of field of 1 mm. When performing cross-correlation analysis between velocity and concentration fields, it is important that the cameras view the same region in space. This requirement was treated as follows. First, images of a calibration target with known dimensions are taken with both cameras. The target consists of a white background with a sequence of squares. The cameras are adjusted so that the magnification is the same and the edges of the squares overlap as closely as possible by adjusting screws on the mounting plate. After this, the calibration target is removed and replaced with a Plexi-glass box filled with water and tracer particles. Images of the tracer particle field are acquired using the Nd:YAG laser for illumination. The two images are then cross correlated with each other using the same interrogation areas and cross-correlation algorithm as in the measurements, which gives the offset between the images in each interrogation cell. After fine-tuning with the adjustment screws, the average offset over the image is 1 pixel with a rms value over the image of 0.24 pixels. In physical space, this means that the spatial bias between the images is limited to 37 μm.

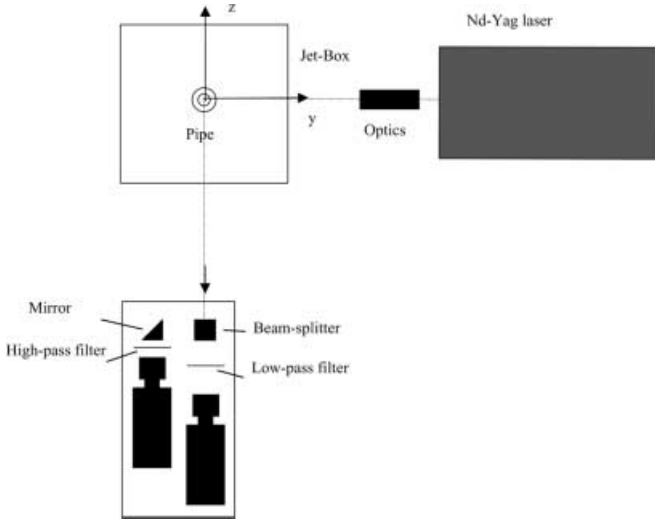

Fig. 4. Top view of the experimental set-up

2.4 Experimental procedure and data processing

The following experimental procedure was used in the collection and processing of the CCD-frames. With the magnification used, one picture covers 3.7 jet diameters. To cover the first six diameters, the jet box is moved vertically with respect to the cameras and the laser. For each position, 80 pictures are taken. These 80 pictures are taken from four different runs with 20 pictures in each run. The reason for this is that the present problem is transient and the molecular tracer concentration and the tank volume increase during the run. For each series, the jet is run for 15 s to allow the jet to develop fully , then 20 pictures are taken with a framing rate of 2 Hz. This procedure generates approximately the same background field with a low concentration (6%) for each run. The flow field changes only slightly during the 10 s when the actual measurements are done. The water surface is elevated by 7 mm during the 10 s when the images are acquired. The influence of this is, however, rather small for the following reasons: The distance from the pipe exit to the surface is long (10 D), the surface velocity is very low (0.1% of the inlet velocity), and the decrease in head is 0.5%, resulting in a change of inlet velocity by 0.3%.

Next, we describe the routine for interpolation of concentration values to the centre of the interrogation cells used in the PIV-analysis. We used the adaptive Gaussian window (AGW) function proposed by Agüi and Jiminez (1986) with the recommended optimal window width. The AGW scheme is given by:

$$\Phi(x^*) = \frac{\sum_{n=1}^{N} \alpha_n \Phi_n}{\sum_{n=1}^{N} \alpha_n}, \qquad \alpha_n = \exp\left(\frac{-(x^* - x^n)^2}{H^2}\right), \quad H = 1.24\delta \tag{10}$$

where Φ is the variable to be interpolated to the position x^*, N is the number of values used in the interpolation,

and H is the window width. The interpolation of concentration to the position where the velocity is stored involves 4×4 pixels on the concentration image (16×16 interrogation area/4 due to overlap and pixel binning), $N = 16$ and δ is equal to the pixel size on the concentration image.

Due to the finite number of samples in the calculation of the turbulent statistics, the error in the estimations of these is not negligible. For the special case where the fluctuating signals are Gaussian white noise processes, analytical expressions for the errors in the estimation of the mean $\overline{\Phi}$, the standard deviation σ_Φ, and the cross-correlation $R_{\Phi\Psi}$ as a function of sample size exists.

The relative uncertainties (ε) in these quantities, respectively, are given by Bendat and Piersol (1986):

$$\begin{array}{ll} \overline{\Phi} & \varepsilon^2 = \frac{1}{N}\left(\frac{\sigma_\Phi}{\overline{\Phi}}\right)^2 \\ \sigma_\Phi & \varepsilon^2 = \frac{1}{2N} \\ R_{\Phi\Psi} & \varepsilon^2 = \frac{1}{N}\left(1 + \frac{1}{(\rho_{\Phi\Psi})^2}\right) \end{array} \tag{11}$$

Typical values for the relative uncertainty ε in our measurements in the shear layers are 3% for mean values, 8% for the standard deviations and 25% for the cross correlation (at a correlation coefficient $\rho_{\Phi\Psi} \approx 0.5$). This is manifested in the measured data, where both mean values and standard deviations are smooth and symmetric, whereas this is not the case for the cross-correlation map. The uncertainty in the cross-correlation is high due to the limited number of samples collected for practical reasons. To reduce the uncertainty in the cross-correlation to around 12% would require 320 images and to reduce it to 5% would require 5,000 images. These estimations have also been verified using data from the numerical simulations.

2.5 Theory and numerical methods

Consider the flow of an incompressible Newtonian fluid, which is governed by the Navier–Stokes equations. In Cartesian tensorial form, they read:

$$\frac{\partial u_j}{\partial x_j} = 0 \tag{12}$$

$$\frac{\partial u_i}{\partial t} + \frac{\partial u_i u_j}{\partial x_j} = -\frac{1}{\rho}\frac{\partial p}{\partial x_i} + \upsilon \frac{\partial}{\partial x_j}\frac{\partial u_i}{\partial x_j} \tag{13}$$

where u_j is the velocity in the j direction, x_j is the coordinate in the j direction, ρ is the density, p is the pressure, and υ is the kinematic viscosity. The evolution of the concentration field is assumed to be:

$$\frac{\partial c}{\partial t} + u_j \frac{\partial c}{\partial x_j} = D \frac{\partial}{\partial x_j}\frac{\partial c}{\partial x_j} \tag{14}$$

where c is the species concentration, u the velocity, t the time and D the diffusion coefficient of the species, which is assumed to be a constant.

Modelling of turbulent flow and mixing involves some kind of filtering in time and/or space. For a variable f, this can be written as

$$\overline{f(x_i,t)} = \int_0^\infty \int_{-\infty}^\infty \int_{-\infty}^\infty \int_{-\infty}^\infty G(x_i - \zeta_i, t-\tau) f(\zeta_i,\tau) \times \mathrm{d}\zeta_1\,\mathrm{d}\zeta_2\,\mathrm{d}\zeta_3\,\mathrm{d}\tau \tag{15}$$

where G is the filter kernel.

The variable f can then be decomposed into a mean and a fluctuating part:

$$f = \overline{f} + f' \tag{16}$$

The Reynolds averaged Navier–Stokes equations (RANS) are based on filtering in time:

$$\overline{f}(x_i) = \lim_{T\to\infty}\frac{1}{T}\int_0^T f(x_i,\tau)\,\mathrm{d}\tau \tag{17}$$

This leads to new unknown terms in the momentum Eqs. (13) and in the concentration Eq. (14) originating from the non-linear terms. The unknown terms in the corresponding RANS equations are

$$\tau_{ij} = \overline{u_i' u_j'} \tag{18}$$

$$\Psi_j = \overline{u_j' c'} \tag{19}$$

The combination of PIV and LIF in a plane can provide three of the six terms in Eq. (18) and two of the three terms in Eq. (19). A common way to model these terms is based on an eddy diffusivity formulation. In analogy to Fick's law for molecular diffusion, the turbulent flux is in the direction of the concentration gradient. The common RANS modelling of Ψ_j is thus

$$\overline{u_j' c'} = -\frac{\nu_t}{Sc_t}\frac{\partial \overline{c}}{\partial x_j} = -D_t \frac{\partial \overline{c}}{\partial x_j} \tag{20}$$

where Sc_t is the turbulent Schmidt number which relates the turbulent diffusivity D_t to the turbulent viscosity ν_t. This type of model is inadequate in more complex situations such as found in combustion where "counter-gradient" diffusion may often be present. More general expressions may be formulated where the turbulent diffusivity is a tensor. If the space filtered approach is applied to Eq. (14), the space filtered concentration evolution equation becomes:

$$\frac{\partial \overline{c}}{\partial t} + \overline{u_j}\frac{\partial \overline{c}}{\partial x_j} = D\frac{\partial}{\partial x_j}\frac{\partial \overline{c}}{\partial x_j} - \frac{\partial \Psi_j}{\partial x_j} \tag{21}$$

where

$$\Psi_j = \overline{u_j c} - \overline{u}_j \overline{c} \tag{22}$$

is the subgrid turbulent flux term which has to be modelled.

The system of the filtered equations, i.e. the momentum and continuity equations and the scalar transport equation (Eq. 21), is discretised on a staggered Cartesian grid. The terms in the equations are approximated by finite differences. All linear terms in the equations (first- and second-order derivatives) are discretised by central schemes. The non-linear convective terms in the momentum equations and the scalar transport equation are discretised by

upwind schemes. Higher-order accuracy is introduced through a single-step defect correction (Fuchs 1984). The spatial accuracy in the present code is $O(h^3)$ for the momentum equations, $O(h^4)$ for the continuity equation and $O(h)$–$O(h^2)$ for the scalar transport equation. The time integration is implicit and second order in time. In each time step, the system of equations is solved iteratively by a multi-grid solver. These numerical techniques have been used for several different LES simulations (Olsson and Fuchs 1996, 1998; Revstedt et al. 1998). These works deal with free or impinging jets, and the effect of different subgrid scale models are investigated. The first two papers deal with dynamic and scale similarity models while, in the third one, SGS-models for both the flow and mixing are considered. It has been shown in these papers that the inclusion of an explicit SGS term has a smaller influence on the mean fields than on the turbulent fluctuation fields and, overall, a rather small influence on the result. In this work, we choose therefore not to use an explicit SGS-model. The fact that the Reynolds number in this investigation is a factor of two lower than in any of the references mentioned above and that the employed spatial resolution is higher gives further support for the present approach. Simulations were made on a sequence of locally refined grids as shown in Fig. 5.

The grids G1–G3 represent global grids, whereas G4–G6 are a sequence of locally refined grids. The mesh spacing of each of the grids in the sequence is half of that of its coarser "parent" grid. The computational geometry is that of a semi-confined jet with large distance to distal the walls, which is a good approximation of the real geometry. At the outlet boundary, the axial gradient of the velocity vector and of the concentration are set to zero. A fundamental problem in most large eddy simulations is the specification of inlet conditions. The most correct way to do this is to perform a time-dependent simulation of the whole inlet geometry together with the flow region by LES or DNS. In the jet flow case under consideration, one may carry out separate simulation of a fully developed turbulent pipe flow from which inlet conditions can be easily extracted. Simplified inlet conditions may be imposed by assuming or computing the spectral content of the turbulence at the inlet and superimpose this on the mean profile. A more sophisticated approach is the one proposed by Na and Moin (1998). The inlet conditions for the velocity are computed through the instantaneous (spatial) field for which the phase information of the fluctuations is preserved, while the amplitude is randomly perturbed. In our computations, we imposed random fluctuations with a flat spectrum. These random perturbations are imposed on a mean velocity profile at the inlet:

$$U(r) = U_{\max}\left(1 - \frac{r}{R}\right)^{0.125}$$

The axial velocity disturbance has random noise with an amplitude of 7% of the mean centreline velocity for $r/R < 0.4$ and 15% for $0.4 < r/R < 0.5$. The disturbance amplitude in the other velocity components is 7% of the mean centreline velocity. The mean velocity profile and the disturbance intensity at the inlet are set to correspond to the measured inlet velocity profile (not shown). The inlet concentration is specified as a top hat profile with zero disturbance level, which seems to be reasonable from a physical point of view, although the measured concentration disturbance level shortly after the inlet is greater than zero. The background concentration is set to 6% of the inlet concentration. The cell distribution on the different grids is given in Table 1.

Grid distribution

In the simulations, the flow is first allowed to develop for 40 time units ($D/U_{\max}$), where one time unit is the time it takes for a particle to travel one diameter with the mean inlet velocity. Turbulent statistics are based on time integration for the following 160 time units corresponding approximately to 160 statistically independent samples. The time-step is 0.02 time units, which corresponds to

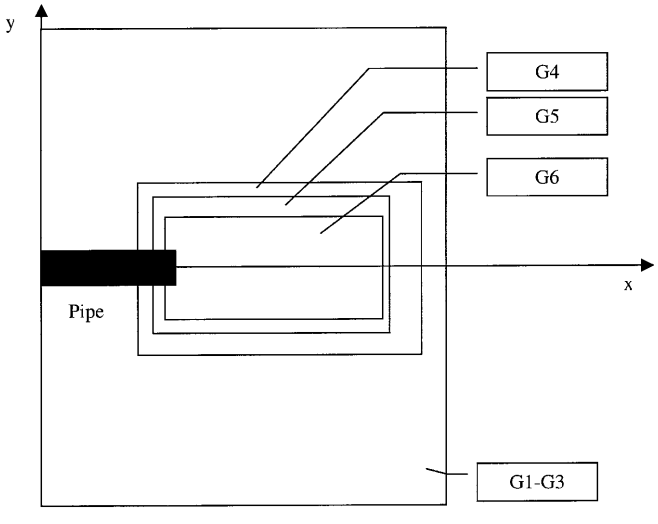

Fig. 5. The computational domain and the extent of the local grids used in the numerical simulation

Table 1. Cell distribution on the different grids

Grid No.	Limits	No. of cells
1	$x/D = -4$ to 8 $y/D = -7$ to 7 $z/D = -7$ to 7	$8 \times 12 \times 12$
2	$x/D = -4$ to 8 $y/D = -7$ to 7 $z/D = -7$ to 7	$16 \times 24 \times 24$
3	$x/D = -4$ to 8 $y/D = -7$ to 7 $z/D = -7$ to 7	$32 \times 48 \times 48$
4	$x/D = -1.5$ to 7.5 $y/D = -2.5$ to 2.5 $z/D = -2.5$ to 2.5	$48 \times 34 \times 34$
5	$x/D = -0.5$ to 6.5 $y/D = -2$ to 2 $z/D = -2$ to 2	$74 \times 54 \times 54$
6	$x/D = -0.2$ to 6.3 $y/D = -1.5$ to 1.5 $z/D = -1.5$ to 1.5	$140 \times 82 \times 82$

0.2 ms. The total number of time-steps is 10,000. The convergence of the statistics was checked across the shear layer six diameters downstream of the inlet and was compared with the error estimates given in Eq. (11). These investigations show that the differences in mean concentration between sample sizes of 80 and 160 samples are smaller than 3%. For the rms values, it is smaller than 8%, and for the cross-correlation of velocity and concentration it is around 20–25% maximum.

3
Results and discussion

Figure 6 shows the instantaneous velocity vector field obtained by DPIV together with the concentration field for the near inlet region of the jet (approximately 0–2.5 diameters downstream of the inlet). One can see that the concentration along the centreline is nearly constant over this distance. The unstable character of the shear layer is clearly visible and rapid mixing takes place immediately after the inlet. The existence of large vortex structures can be seen, which act to entrain fluid with low concentration into the jet. These structures appear very close to the inlet and are coupled to the instability mechanisms discussed in the introduction. As pointed out by Crow and Champagne (1971), the development of these structures is sensitive to certain perturbation frequencies and their amplitude at the inlet. In their experiments, perturbations at and close to the most amplified mode [Strouhal number (St) $\sim$ 0.3] resulted in an earlier and stronger decrease in the mean velocity along the centre line. As the inlet flow is a fully developed turbulent pipe flow, the disturbances in this case represent a continuous spectrum of frequencies. For nozzle flows, the region close to the inlet, where the velocity along the centreline is unaffected, is named the potential core due to its nearly irrotational character. We name this the core region, even though in this case it contains small-scale turbulence.

Figure 7 shows the field of ensemble concentration fluctuation field. The width of the annular shear-layer grows as the distance from the inlet increases and in our case the layer becomes circular at approximately three diameters downstream of the inlet. In the core, the fluctuation levels are low compared with the shear layers.

3.1
Comparison with earlier experimental results

The experimental work of Lemoine et al. (1996) is the one found in the literature which is closest to the present one in terms of inlet Reynolds number and flow configuration. Although they primarily investigate the flow in the self-similar far field region of the jet, they provide mean velocity and mean concentration profiles some diameters downstream of the inlet. The main differences in the present work is that we used a fully developed turbulent profile at the inlet, whereas they used a "top-hat"-like nozzle flow, and that they have a very slow co-flow around the jet. Figure 8 shows a comparison for normalised mean axial velocity at $x/D = 4$, and Fig. 9 shows the normalised mean concentration at the same axial position. The normalised mean axial velocity and the normalised mean concentration are defined as:

$$U^* = \frac{\overline{u(x,y)}}{\overline{u(x,0)}} \quad C^* = \frac{\overline{c(x,y)}}{\overline{c(x,0)}}$$

The radial distance was normalised by the half-width radius for velocity and concentration denoted by r_v and r_c, respectively, and the sampling distance is defined by the following relations:

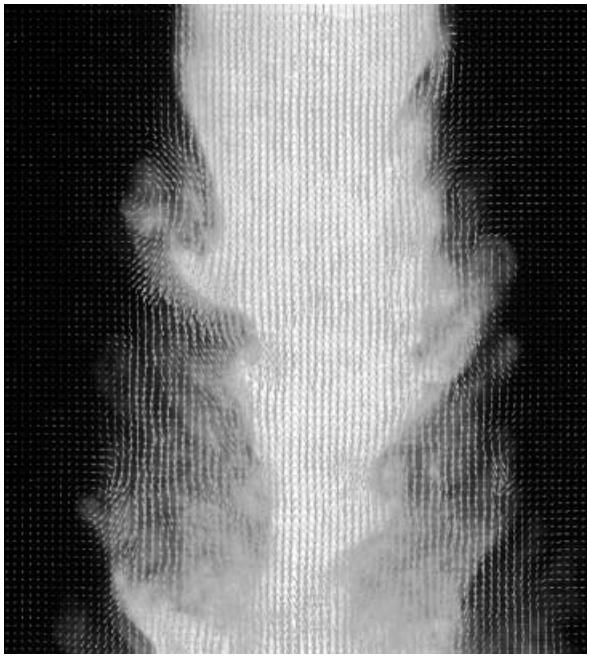

Fig. 6. Instantaneous velocity-vector and concentration fields (0–2.5 D)

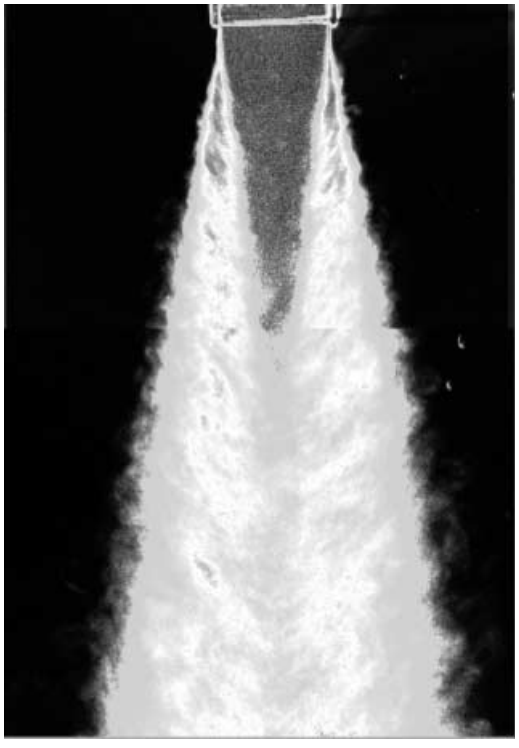

Fig. 7. Mean concentration fluctuations

$$U^*(x, r_v) = \tfrac{1}{2} \quad C^*(x, r_c) = \tfrac{1}{2}$$
$$y^* = \frac{y}{r_v} \qquad y^* = \frac{y}{r_c}$$

It can be seen that both the velocity and the concentration profiles agree rather well.

The concentration in our experiment settles at around 6% of its maximum value due to the background concentration present in the experiment. The scaling used above is normally applied in the self-similar region where appropriately scaled results, taken at different downstream positions, overlap. Mean velocity and mean concentration fields reach self-similarity very quickly after the shear layers have merged, and we have observed that self-similarity in the mean variables is almost obtained after $x/D = 4$.

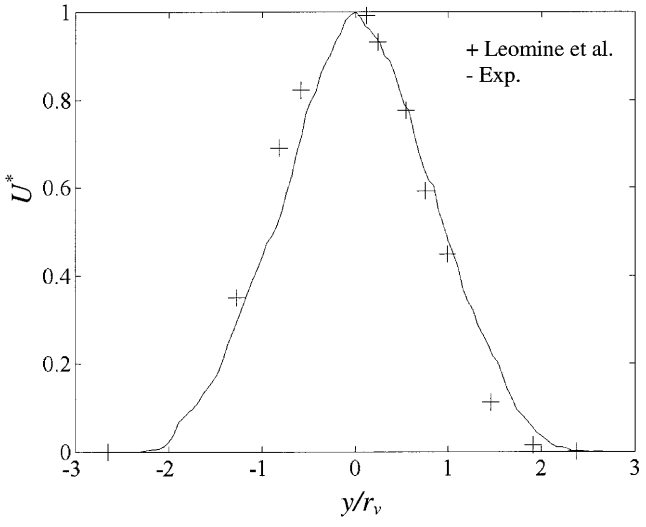

Fig. 8. Non-dimensional mean axial velocity at $x/D = 4$; also the experimental results of Lemoine et al. (1996)

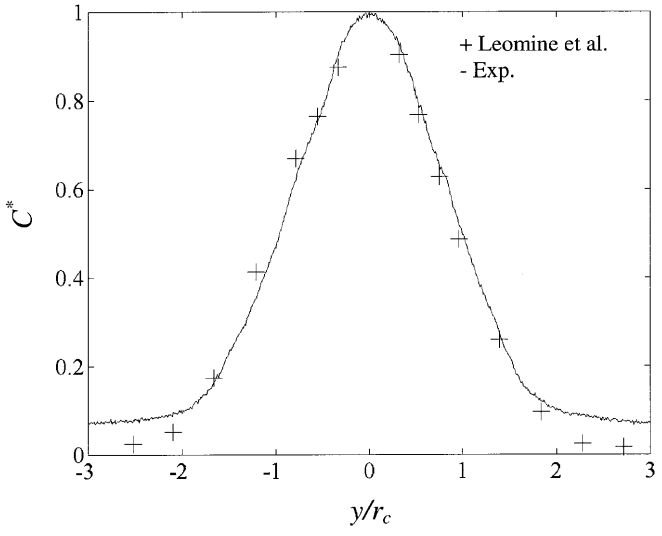

Fig. 9. Non-dimensional mean concentration at $x/D = 4$; also the experiments of Lemoine et al. (1996)

3.2
Comparison with numerical simulations

Numerical and experimental results were compared along the centre-line. The experimental and numerical results agree well with a slightly larger deviation for the mean concentration. The core region extends to approximately three diameters downstream of the inlet.

Both numerical and experimental data show a nearly constant level of fluctuation for both velocity and concentration in the core. The disturbance level in the core for the velocity fluctuations are higher than the concentration fluctuations due to the fully developed turbulent pipe flow. We note that the random noise imposed at the inlet on the mean flow profile in the numerical simulations decrease slightly in the core region. Concentration fluctuations evolve in roughly the same manner as the velocity fluctuations. The fluctuation level for concentration is low in the core region, and the end of the core is characterised by a rapid increase in fluctuation levels, which is captured well by the numerical simulation.

3.2.1
Radial profiles

Consider the radial mean profiles for velocity and concentration, respectively. Figure 10 shows mean profiles for axial velocity at three downstream locations. The agreement between measured and simulated profiles is good. The same holds for the concentration profiles shown in Fig. 11, with a slightly larger deviation for the position $x/D = 4$.

Next we examine turbulent stresses and turbulent concentration fluctuations at different downstream locations.

Figure 12 shows the radial distribution of axial velocity fluctuations normalised with the inlet centreline velocity at three different downstream positions, and Fig. 13 shows the turbulent shear stress, normalised with the square of

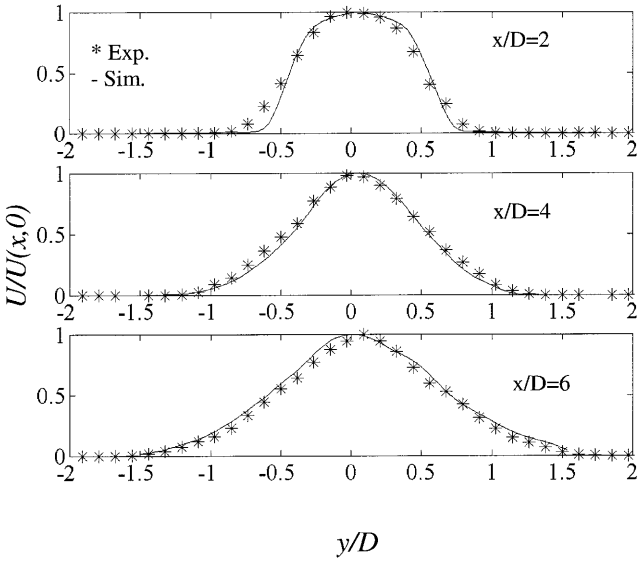

Fig. 10. Radial profiles of the mean axial velocity at three different positions along the jet centreline: *upper chart*, $x/D = 2$; *middle chart*, $x/D = 4$; *lower chart*, $x/D = 6$

the inlet centreline velocity for the same locations $\left(\tau_{xy}/U_{\text{in}}U_{\text{in}} = \overline{u'v'}/U_{\text{in}}U_{\text{in}}\right)$.

The levels of axial velocity fluctuations obtained from experiments and numerical simulations agree well. This good agreement is, however, a little bit illusory because, as shown in Fig. 13, the level of turbulent shear in the numerical results is significantly lower at the position closest to the nozzle. Qualitatively, the evolution of both the axial velocity fluctuations and the turbulent shear is different for the numerical simulations and the experiments. This is attributed to the boundary condition imposed on the velocity fluctuations at the inlet. The resolution of the shear-layer at the inlet may also play some role in the discrepancy. In the experiments, both velocity fluctuations and the turbulent shear have a maximum very close to the inlet $(x/D) < 1$, which is followed by a decrease further downstream. This behaviour was also observed by Sami et al. (1967) for nozzle flow with a Reynolds number of 22 000. The numerical results show a delayed growth of fluctuations in the shear layer and a maximum for $(x/D) > 2$. In spite of this, the levels and shapes agree very well for $x/D = 4$ and $x/D = 6$. Figure 14 shows the levels of concentration fluctuations across the shear layer at $x/D = 2$,4 and 6, respectively. These profiles show the same behaviour as the velocity fluctuations but do not agree equally well in their magnitude. The shapes and degree of radial spreading agree well but the peak levels in the mixing layer differ by as much as 30%. Similar qualitative behaviour is observed for the velocity fluctuations; namely, the experiments show maxima in the shear layers very close to the inlet, whereas the numerical analyses show a delayed growth and larger peak values.

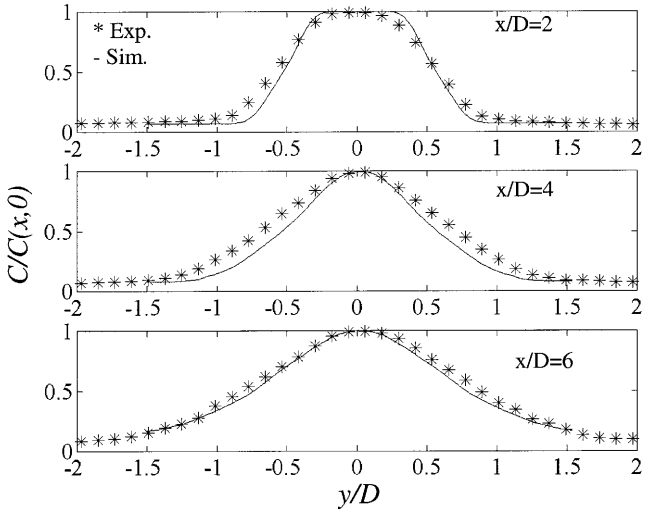

Fig. 11. Radial profiles of the mean concentration field at three different positions along the jet centreline: *upper chart*, $x/D = 2$; *middle chart*, $x/D = 4$; *lower chart*, $x/D = 6$

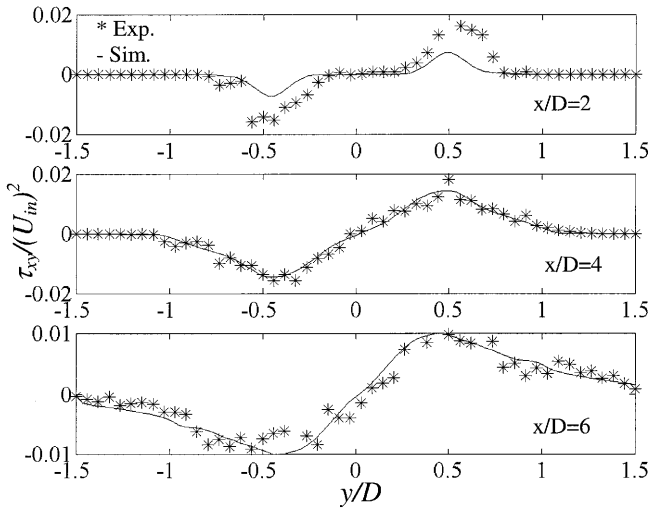

Fig. 13. Radial profiles of the Reynolds shear stress at three different positions along the jet centreline: *upper chart*, $x/D = 2$; *middle chart*, $x/D = 4$; *lower chart*, $x/D = 6$

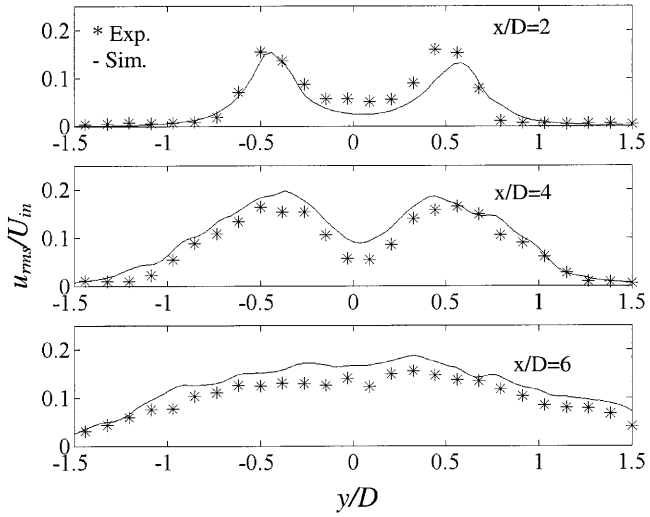

Fig. 12. Radial profiles of the axial velocity fluctuations at three different positions along the jet centreline: *upper chart*, $x/D = 2$; *middle chart*, $x/D = 4$; *lower chart*, $x/D = 6$

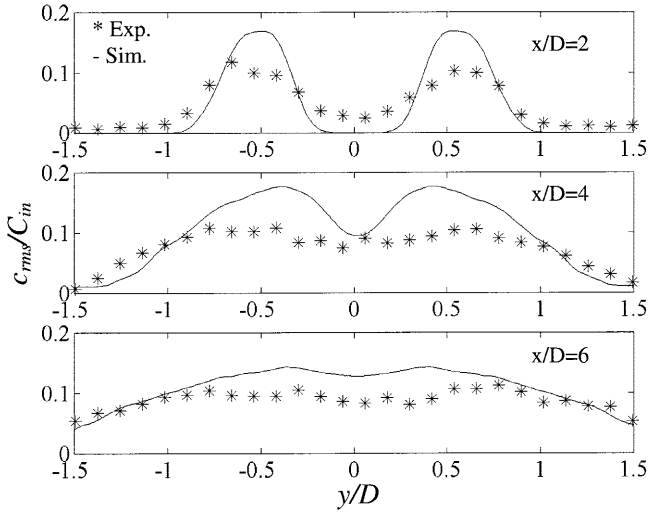

Fig. 14. Radial profiles of the concentration fluctuations for three different positions along the jet centreline: *upper chart*, $x/D = 2$; *middle chart*, $x/D = 4$; *lower chart*, $x/D = 6$

The most interesting variables that can be obtained from the simultaneous measurements of velocity and concentration are the turbulent mass transport terms. Figure 15 depicts the radial distribution of the turbulent concentration flux in the radial direction normalised with the inlet centreline velocity and the inlet concentration. The profile is anti-symmetric and shows peaks in the shear layers. Note that, in Fig. 15, numerical results are presented for $y/D < 0$ and experimental results for $y/D > 0$.

The shapes and radial spreading are similar but, quantitatively, the difference is as large as 50% between numerical and experimental data. The good agreement of the shapes and radial spreading is shown in Fig. 16, which presents the same data as in Fig. 15 but each set was normalised with its maximum value to facilitate comparison.

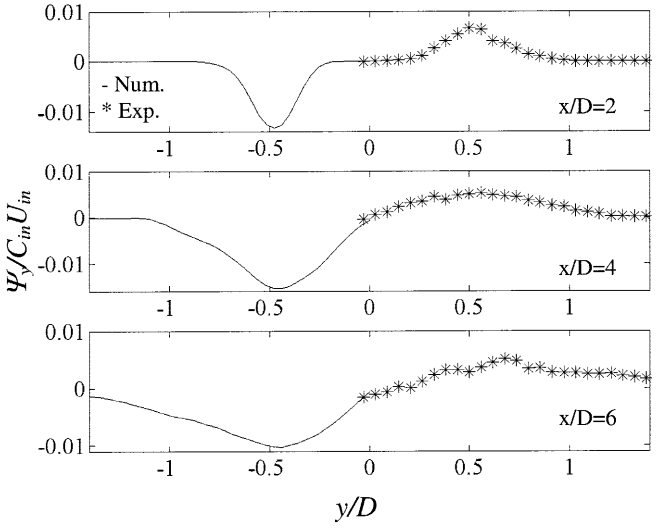

Fig. 15. Radial profiles of the radial turbulent flux of the tracer at three different positions along the jet centreline: *upper chart*, $x/D = 2$; *middle chart*, $x/D = 4$; *lower chart*, $x/D = 6$. Numerical results are shown for $y/D < 0$ and experimental results for $y/D > 0$

It can also be seen that the agreement in the magnitudes improves further downstream of the inlet. It can be confirmed that the main difference in the results comes from the magnitude difference in the velocity and concentration fluctuations and is not due to a significant lower correlation between fluctuating velocity and fluctuating concentration. This is achieved by considering the normalised correlation coefficient for the radial-velocity and concentration fluctuations ρ_{vc}, defined as:

$$\rho_{vc} = \frac{\overline{v'c'}}{\sqrt{\overline{v'^2}}\sqrt{\overline{c'^2}}}$$

This variable is always between −1 and 1. The radial variation in ρ_{vc} for the experimental and the numerical data is shown for the position $x/D = 6$ in Fig. 17. The experimental correlation coefficient has no expressed tendency of being lower than the corresponding numerical data. This observation supports the assertion that the difference in absolute values is due to lower measured amplitude of the fluctuations in velocity and concentration.

For completeness we also present the turbulent concentration flux in the axial direction. The radial distribution of the turbulent concentration flux in the axial direction normalised with the peak value at that position is presented in Fig. 18. This profile is symmetric, and shows the same tendency as that observed for the turbulent concentration flux in the radial direction. A rather good agreement of the shapes and radial spreading between experimental and numerical data can be seen.

3.3
Turbulent diffusivity

As discussed in Sect. 2.5, a usual way to model the turbulent species flux in RANS models is by the gradient diffusion model Eq. (20). In the measurements, we have access to two of the components in this equation, namely the axial and the radial components. If this were an ideal model, the calculation of the turbulent diffusivity from the

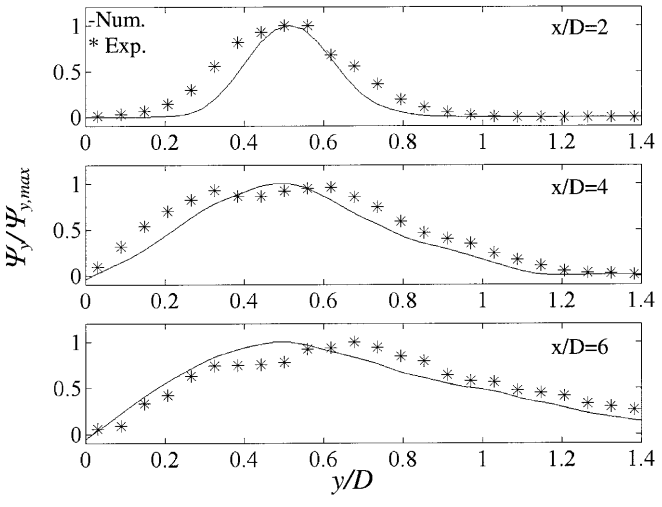

Fig. 16. Radial profiles of the radial turbulent flux of the tracer normalised with their respective peak values

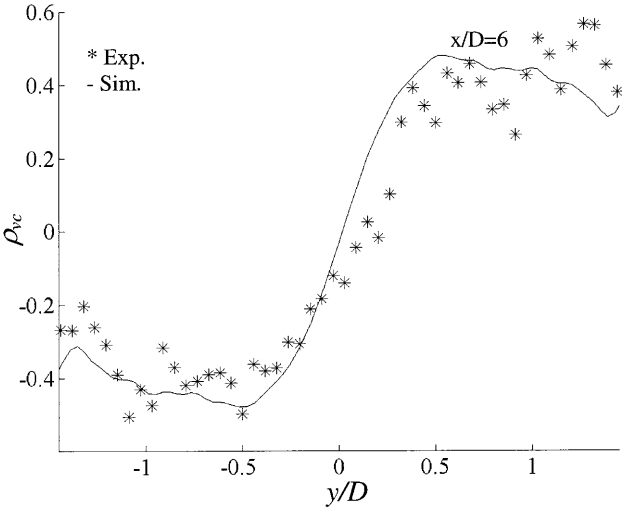

Fig. 17. Radial profile of the correlation coefficient for radial velocity–concentration correlation at $x/D = 6$

axial and radial turbulent mass transport would end up with the same turbulent diffusivity. Figure 19 shows the turbulent diffusivity calculated by the radial transport term:

$$\overline{v'c'} = -D_t \frac{\partial \overline{c}}{\partial y}$$

for the axial positions $x/D = 2$,4 and 6, respectively.

In the upper chart, the numerical results are shown for $y/D < 0$ and results obtained from experimental data are shown for $y/D > 0$. Due to numerical difficulties when the mean concentration derivative is small, the curves are not shown close to $y = 0$. The lower chart depicts the eddy mass diffusivity normalised with its maximum value at each axial location to facilitate the comparison of the shape and radial distribution. The turbulent mass diffusivity obtained from the turbulent concentration flux in the radial direction is positive and symmetric. It increases in the axial direction due to the faster decay of the mean concentration gradient than the velocity–concentration correlation. The magnitude of the eddy mass diffusivity is approximately 100 times larger than the kinematic viscosity of water. The radial distribution is similar to the velocity fluctuation profile, which is reasonable from a modelling point of view. In the k–ε model, the turbulent diffusivity is proportional to k^2/ε, where k is the kinetic energy and ε is the dissipation rate. This quantity is proportional to the velocity fluctuations multiplied by a turbulent length scale. This would imply (for a slowly varying turbulent length scale) that the profile of D_t would be close to that of the velocity fluctuations. If instead we determine the turbulent diffusivity from the axial component:

$$\overline{u'c'} = -D_t \frac{\partial \overline{c}}{\partial x}$$

the picture is completely different. This is shown for the location $x/D = 6$ in Fig. 20.

The magnitude is now approximately ten times larger (the axial turbulent mass flux has approximately the same magnitude in the peaks, but the axial concentration gradient is smaller). The most striking thing, however, is that at the edges of the jet the turbulent diffusivity is negative. This occurs because, as the dye spreads in the radial direction as it moves downstream, the axial concentration gradient becomes positive near the edges of the jet, but the velocity-concentration correlation in the axial direction is also positive. Thus near the edges of the jet, "countergradient" diffusion occurs. This cannot be modelled by a simple gradient diffusion model.

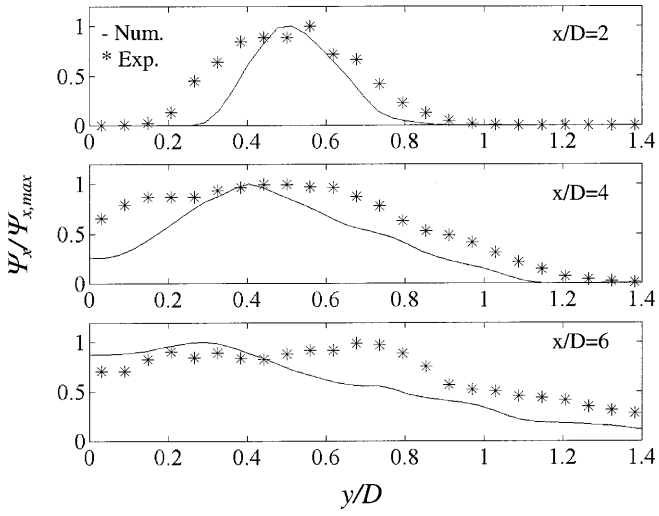

Fig. 18. Radial profiles of the axial turbulent flux of the tracer: experiments and numerical simulations normalised with their respective peak values

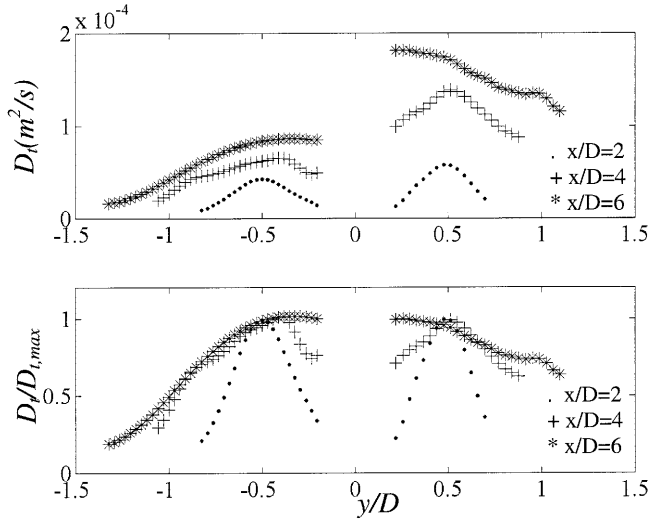

Fig. 19. Turbulent mass-diffusivity computed from the radial velocity–concentration correlation and the radial concentration gradient. The *upper chart* shows the turbulent mass-diffusivity in dimensional form [m^2/s]: experiments (*left*) and numerical simulations (*right*). In the *lower chart* the turbulent diffusivity is normalised with its peak value in each cross-section, experiments for ($y/D < 0$) and numerical simulations for ($y/D > 0$)

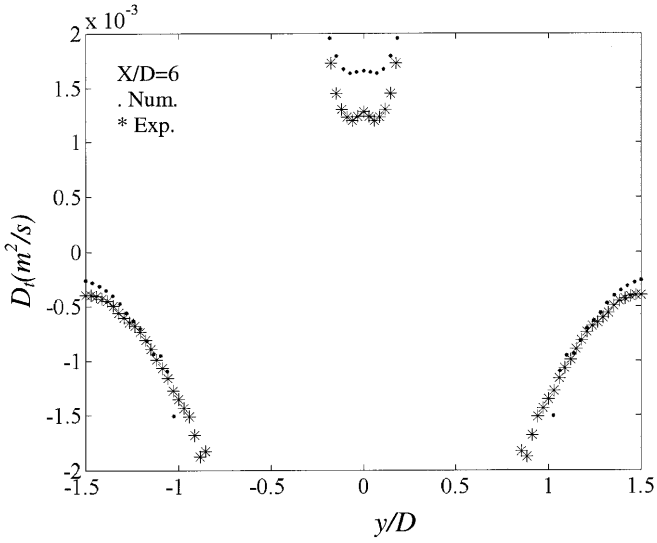

Fig. 20. Turbulent diffusivity computed from the axial velocity-concentration correlation and the axial concentration gradient

4
Concluding remarks

A method for the simultaneous measurement of velocity and concentration by PIV and PLIF was developed and successfully applied to the near inlet region of a spatially developing turbulent jet. A procedure for checking the overlap of the images of the concentration field and the particle field was presented as well as the interpolation scheme used to obtain the concentration and velocity at the same spatial location. This is necessary for the determination of the cross-correlation between velocity and concentration with good accuracy. Turbulent statistics for velocity and concentration including the cross-correlation between velocity and concentration fluctuations were determined for the first six diameters downstream of the inlet. The experimental data were compared with earlier experimental data and large eddy simulations of the flow. The general agreement between experiments and simulations was found to be good. The mean centreline velocity and concentration along the centreline agree well. The same holds for the growth of velocity and concentration fluctuations along the centreline. Radial profiles of mean axial velocity agree well both with earlier experiments and with the current simulations. Differences between measured and simulated quantities are found mainly in radial distribution of the concentration fluctuations, for which the experiment data have a lower level. Together with the slightly lower values in velocity fluctuations this gives a significant difference in turbulent mass transport terms. However, the agreement of the velocity–concentration correlation coefficient is good, which is attributed to the normalisation that eliminates the scaling problem. Also, if better accuracy of the fluctuating quantities is desired, larger samples of data must be used. Conceptual problems for a turbulent mass transport model based on gradient diffusion with a scalar turbulent mass diffusivity are pointed out by the aid of the experimental data.

References

Agüi JC; Jiminez J (1987) On the performance of particle tracking. J Fluid Mech 185: 447–468

Bendat JS; Piersol AG (1986) Random data (analysis and measurement procedures). John Wiley, New York

Crow SC; Champagne FH (1971) Ordered structure in jet turbulence. J Fluid Mech 48: 547–591

Danaila I; Dušek J; Fabien A (1997) Coherent structures in a round, spatially evolving, unforced, homogenous jet at low Reynolds numbers. Phys Fluids 9: 3323–3342

Fuchs L (1984) Defect-corrections and higher numerical accuracy. In: Hackbusch W (ed) Proceedings of the GAMM-workshop on "Efficient Solvers for Elliptic Systems", Notes Numer Methods Fluid Mech 10: 52–66

Karasso PS; Mungal MG (1997) PLIF measurements in aqueous flows using the Nd: YAG. Exp Fluids 23: 382–387

Lemoine F; Wolff M; Lebouche M (1996) Simultaneous concentration and velocity measurements using laser-induced fluorescence and laser Doppler velocimetry: application to turbulent transport. Exp Fluids 20: 319–327

Liu S; Meneveau C; Katz J (1994) On the properties of similarity subgrid-scale models as deduced from measurements in a turbulent jet. J Fluid Mech 275: 83–119

Na Y; Moin P (1998) Direct numerical simulation of a separated turbulent boundary layer. J Fluid Mech 370: 175–201

Olsson M; Fuchs L (1996) Large eddy simulations of the proximal region of a spatially developing circular jet. Phys Fluids 8: 2125–2137

Olsson M; Fuchs L (1998) Large eddy simulations of a forced semi-confined circular impinging jet. Phys Fluids 10: 476–486

Raffel M; Willert C; Kompenhans J (1998) Particle image velocimetry – a practical guide. Springer, Berlin Heidelberg New York

Revstedt J; Gullbrand J; Guillard F; Fuchs L; Trägårdh C (1998) Large eddy simulations of mixing in an impinging jet. In: Papailiou KD, et al (eds) Proceedings of the 4th ECCOMAS computational fluid dynamics conference. John Wiley, New York

Sakakibara J; Hishida K; Maeda M (1997) Vortex structure and heat transfer in the stagnation region of an impinging plane jet (simultaneous measurements of velocity and temperature fields by digital particle image velocimetry and laser induced fluorescence). Int J Heat Mass Transfer 40: 3163–3176

Sami S; Carmody T; Rouse H (1967) Jet diffusion in the region of jet-flow establishment. J Fluid Mech 27: 231–252

van Cruyningen I; Lazano A; Hanson RK (1990) Quantitative imaging of concentration by planar laser-induced fluorescence. Exp Fluids 10: 41–49

Westerweel J; Dabiri D; Gharib M (1997) The effect of a discrete window offset on the accuracy of cross-correlation analysis of digital PIV recordings. Exp Fluids 23: 20–28